Nonisothermal drop impact and evaporation on polymer nanofiber mats

Christina M. Weickgenannt, Yiyun Zhang, Andreas N. Lembach, Ilia V. Roisman, Tatiana Gambaryan-Roisman, Alexander L. Yarin, and Cameron Tropea

Phys. Rev. E **83**, 036305 — Published 11 March 2011
DOI: 10.1103/PhysRevE.83.036305

Non-isothermal drop impact and evaporation on polymer nanofiber mats

Christina M. Weickgenannt, [1, 2] Yiyun Zhang, [3] Andreas N. Lembach,[1,2] Ilia V. Roisman, [1, 2]

Tatiana Gambaryan-Roisman, [2, 4] Alexander L. Yarin, [2, 3, *]and Cameron Tropea[1, 2, †]

[1] *Institute of Fluid Mechanics and Aerodynamics*

Technische Universität Darmstadt, 64287 Darmstadt, Germany

[2] *Center of Smart Interfaces*

Technische Universität Darmstadt, 64287 Darmstadt, Germany

[3] *Department of Mechanical and Industrial Engineering*

University of Illinois at Chicago, MC 251 Chicago, Illinois 60607-7022, U.S.A.

[4] *Institute for Technical Thermodynamics*

Technische Universität Darmstadt, 64287 Darmstadt, Germany

Abstract

The work describes the experimental and theoretical investigation of water drop impact onto electrospun polymer nanofiber mats deposited on heated stainless steel foils. The measurements encompass water spreading over and inside the mat, as well as the corresponding thermal field. The results show that the presence of polymer nanofiber mats prevents receding motion of drops after their complete spreading and promotes the moisture spreading inside the mat over a large area of the heater, which facilitates a tenfold enhancement of heat removal as the latent heat of drop evaporation.

PACS numbers: 44.35.+c, 47.55.dr, 47.56.+r

* ayarin@uic.edu

† ctropea@sla.tu-darmstadt.de

1. INTRODUCTION

The continuously rising demand for faster central processing units, the miniaturization and breakthrough developments in the field of semiconductor, optical and radiological components and the emergence of unmanned aerial and ground vehicles (UAVs and UGVs) result in a growing need for more powerful cooling technologies. These must be capable of removing heat fluxes of up to 1 kW/cm^2. Among the different approaches to cooling, which include, for example, natural and forced convection, heat pipes or micro-channel heat sinks, spray cooling is presently one of the most promising methods [1-7]. The tremendous cooling potential of spray cooling is associated with liquid evaporation at the hot surface. Thereby the efficiency is strongly affected by the hydrodynamics and heat transfer associated with drop impact onto hot surfaces. However, the typical receding motion of the spread-out liquid lamellae on hot metal surfaces leads to complete drop bouncing and interruption of cooling in many cases. Moreover, due to the insulating vapor layer established between the drop and the surface the heat flux reduces significantly in the Leidenfrost regime at higher temperatures.

A novel approach in drop and spray cooling of microelectronic devices employs coating of hot surfaces with electrospun non-woven polymer nanofiber mats [8, 9]. Electrospun nanofiber mats are nano-textured permeable materials comprising of individual polymer nanofibers (with diameter of about several hundred nanometers) which are randomly orientated in the mat plane. The size of the inter-fiber pores is of the order of several micrometers, and mat thickness can be several hundred microns. The electrospun nanofiber mats are usually produced from polymers which are either partially wettable or nonwettable [10, 11].

The benefits of using nanofiber mats in drop and spray cooling applications are mainly based on their influence on the hydrodynamic behavior of the impacting drops, as well as an increased heat transfer area. Previous observations showed essentially two significant features of drop impact on nanofiber mats [9]. First of all, receding, splashing and bouncing during the impact on polymer nanofiber mats seem to be practically eliminated. Drop spreading after impact is similar to that on an impermeable surface, but the drop contact line is pinned as the maximum spread diameter reached. Second, drop spreading is accompanied by a filling of the pores, which are almost instantaneously impregnated underneath the area encircled by the pinned contact line. Pores continue to be filled after the contact line has been arrested, and liquid spreads inside the nanofiber mat over an area significantly larger than the one encircled by the pinned contact line. Both features lead to an enhancement of heat transfer due to the enlargement of the contact area between water and the underlying hot surface. Moreover, nanofiber mats possess tremendously large surface area of about 10^5 m^2/g, which also facilitates heat removal.

The present work aims at a detailed elucidation of the drop spreading behavior above and inside nanofiber mats. The evolution of the wetted spot (the water spreading area inside nanofiber mats after drop impact), the corresponding temperature distribution at the heated foil as well as the evaporation time have been measured for different thicknesses of the mats, different initial temperatures of the hot surface and different drop impact velocities. A physical interpretation of the results and physical insights into the governing mechanisms are also provided.

2. EXPERIMENTAL METHOD AND DATA PROCESSING

A. Experimental setup

Nanofiber mats used in the present experiments were electrospun from PAN [poly(acrylonitrile)], a partially wettable polymer with a water contact angle on a cast sample of about 30 - 40 °C and from PAN containing carbon black nanoparticles (CB), which tends to increase roughness of individual nanofibers [12]. Square samples of nanofiber mats with a side length of about 4 cm, thickness of the order of several hundred micrometers and porosity of the order of 90-95 % were produced. Nanofiber mats were electrospun on stainless steel foils attached to a grounded electrode. The thickness of the foils was 50 μm. The electrospinning process is described elsewhere [10, 11, 13]. Typical scanning electron microscope images of the nanofibers used in the experiments are shown in Figs. 1 and 2.

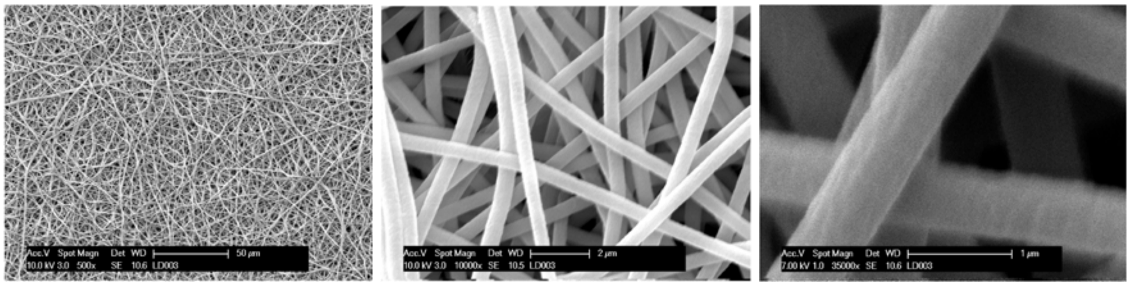

FIG. 1. Scanning electron microscope images of PAN nanofibers at various magnifications

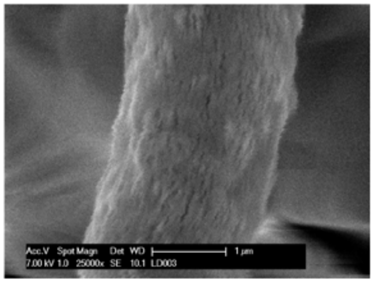

FIG. 2. Scanning electron microscope image of a PAN fiber containing carbon black nanoparticles.

A schematic diagram of the experimental setup for drop impact is shown in Fig. 3. It consists of the following main elements: drop generation system, impingement surface (stainless steel foil covered by nanofiber mat), heating system, high-speed imaging and illumination system and an infrared imaging system. For drop generation a medical syringe with a stainless steel needle was used. The needle was flat tipped. The syringe was manually operated in such a way that a drop could form at the needle tip, detach under its own weight and be accelerated by gravity. The initial drop diameter was d_0 = 2 mm ± 0.3 mm**.** The syringe was fixed at a vertical adjusting spindle, which allowed varying the height of the needle tip over the target surface. The varied impact heights were H = 5 cm, 15 cm and 50 cm, which correspond to the following impact velocities respectively: $V_0 \approx 1$ m/s, 1.7 m/s and 3 m/s.

The stainless steel foils covered by nanofiber mats were heated electrically. The lower surfaces of the foils have been coated with black graphitic spray. Such coating improves the temperature measurement of the foil using the infrared technique. A special mounting device provided continuous stretching of the foil, necessary for compensation of the effects related to the foil thermal expansion at elevated temperatures. The mounting device also incorporated an integrated electric heating system. To ensure small contact resistance, copper plates pressed on the foil from below were used as connections.

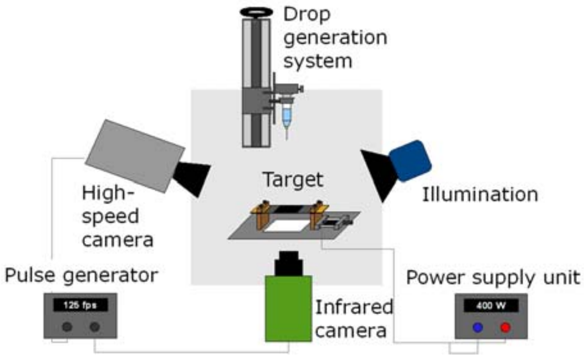

FIG. 3. Experimental setup for drop impact onto nanofiber mats.

A high-speed CCD camera (Photron's Fastcam 1024 PCI) with a framerate of 1,000 fps recording at 1024 x 1024 image resolution was used to observe the shape of the spreading drop above the hot surface and to measure the initial drop diameter and impact velocity. The camera was aligned at an angle of 40° with respect to the horizontal. The observability of the subsequent drop spreading inside the nanofiber mats depends on several conditions. In general, the refractive indices of the polymer nanofibers and water are such that if a certain level of moisture concentration is reached in the nanofiber mat, it becomes transparent and the underlying darker steel surface becomes visible through the nanofiber mat. Then, water spreading inside the nanofiber mat can be observed as a growing dark area. However, this method is only successful for relatively thin mats and fails in the case of thicker mats [9].

For this reason a second observation technique was used in these experiments. An infrared camera (Thermosensorik's CMT 256 M HS) with a refresh rate of 885 Hz in full-frame mode and thermal resolution of < 10 mK was positioned underneath the targets and recorded the temperature distribution at the reverse side of the steel foils. The moisture contained inside the mat evaporates leading to the foil cooling. Since the foils are very thin (50 μm) the moisture containing area of the mats coincided with the cooled area of the steel foil at any time instant of the water spreading (see Section IIC)**.** In this way the liquid spreading could be identified for various mat thicknesses. The two cameras, CCD and infrared, were synchronized to achieve simultaneous drop imaging and thermal measurements.

The data from the images were analyzed using an image processing code programmed in Matlab. For this purpose the raw data of the infrared camera were converted into temperature levels using calibration curves for each foil used. The image intensity was assumed to be related to the radiation heat flux when using the raw data/temperature curve. According to the Stefan-Boltzmann law, the heat flux transferred from a hot body to a cold body is proportional to the difference of the fourth powers of the surface temperatures. The 1/4 power law was thus chosen to fit the calibration data.

A series of experiments were performed using the setup described at initial foil temperatures ranging from 60 °C to 120 °C with an increment of 20 °C. Each drop impact experiment started after the foil (heated by the electric current) reached a steady temperature. For the measurement of the initial foil temperature, an external, calibrated thermocouple, which was pressed manually onto the foil, was used. For each foil and at each temperature a reference sequence was first recorded, which was needed for the computation of the calibration curves to convert the raw intensity data of the infrared camera into temperature values. After that, a single drop impacted onto the nanofiber mat and the entire spreading and evaporation process was recorded at a low frequency of 125 Hz, simultaneously by both camera systems (CCD and the infrared camera). Additionally the drop impact sequence was recorded only by the CCD camera with a frequency of 30000 Hz.

The thermal resolution of the infrared camera was limited by a temperature of 120 °C. At higher foil temperatures (up to 300°C) a single thermocouple of type K with diameter of 0.5 mm was used for temperature measurements. It was positioned right underneath the impact point of the drop and fixed mechanically, which resulted in a measuring error of about 4 °C. The experimental procedure was the same as described before.

B. Typical phenomena of drop impact, spreading and evaporation

Figure 4 shows typical CCD images of drop impact on a bare steel foil as well as on a steel foil coated with a PAN nanofiber mat of thickness $h=1.05$ mm. In both cases (bare steel and steel coated with nanofibers) the initial foil temperature was about 60 °C and the drop impact height was $H = 15$ cm. The drop impact onto a smooth bare steel substrate is followed by spreading and receding of liquid over the surface as expected [14] (see Fig. 4, top). After the receding stage the liquid drop reaches a quasi-steady state. The observed behavior during the first few milliseconds after drop impact onto a nanofiber mat is very similar to that in the case of a bare steel foil (see Fig. 4, bottom). The drop first spreads on the polymer mat as on a dry and impermeable smooth rigid surface. However, at the end of the spreading stage the contact line of the drop appears to be pinned in the spread-out configuration and does not recede [9].

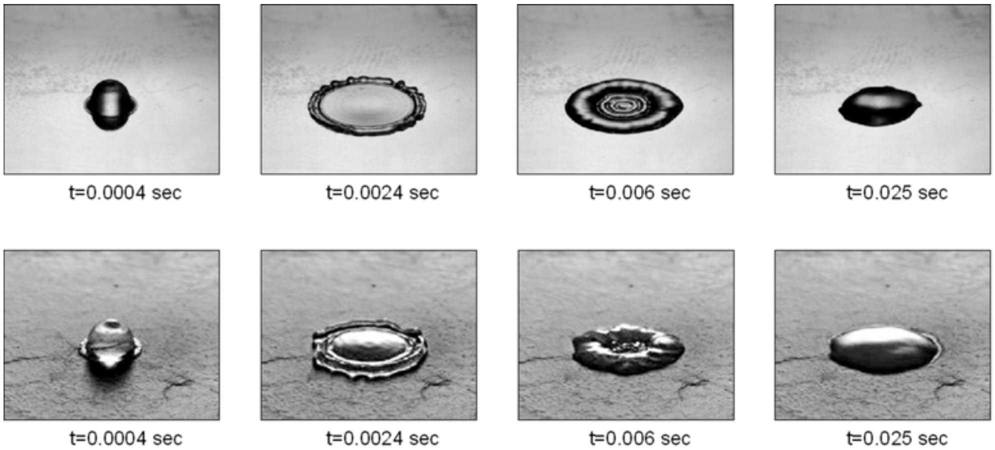
t=0.0004 sec t=0.0024 sec t=0.006 sec t=0.025 sec

t=0.0004 sec t=0.0024 sec t=0.006 sec t=0.025 sec

FIG. 4. Drop impact on a bare steel foil and on a nanofiber mat at a foil temperature of 60°C. Top: bare steel; bottom: steel foil covered with PAN nanofiber mat (mat thickness h=1.05 mm).

Figure 5 demonstrates the differences between drop evaporation on a bare steel foil and on a steel foil coated with a nanofiber mat. Five typical CCD frames and the corresponding infrared images from below are shown. Due to the low recording frequency of 125 Hz, the initial stage of drop impact could not be observed in full detail. The nanofiber mat, the initial foil temperature, as well as the impact height, were the same as in the example shown in Figure 4. In the case of a bare steel foil, the drop reached a quasi-steady state after the initial liquid motion came to rest, as is seen in Fig. 5 (a.1). In the following process, the drop contact line remains practically pinned over a significant fraction of the drop lifetime. In contrast to that, the drop height and the contact angle both continually decrease, because of the mass loss due to evaporation. Only near the end of the evaporation process does the contact line show an appreciable shrinkage. The temperature of the cooled area underneath the drop stays nearly constant as long as the evaporation lasts, as it can be seen in Figs. 5 (a.3) - (a.5).

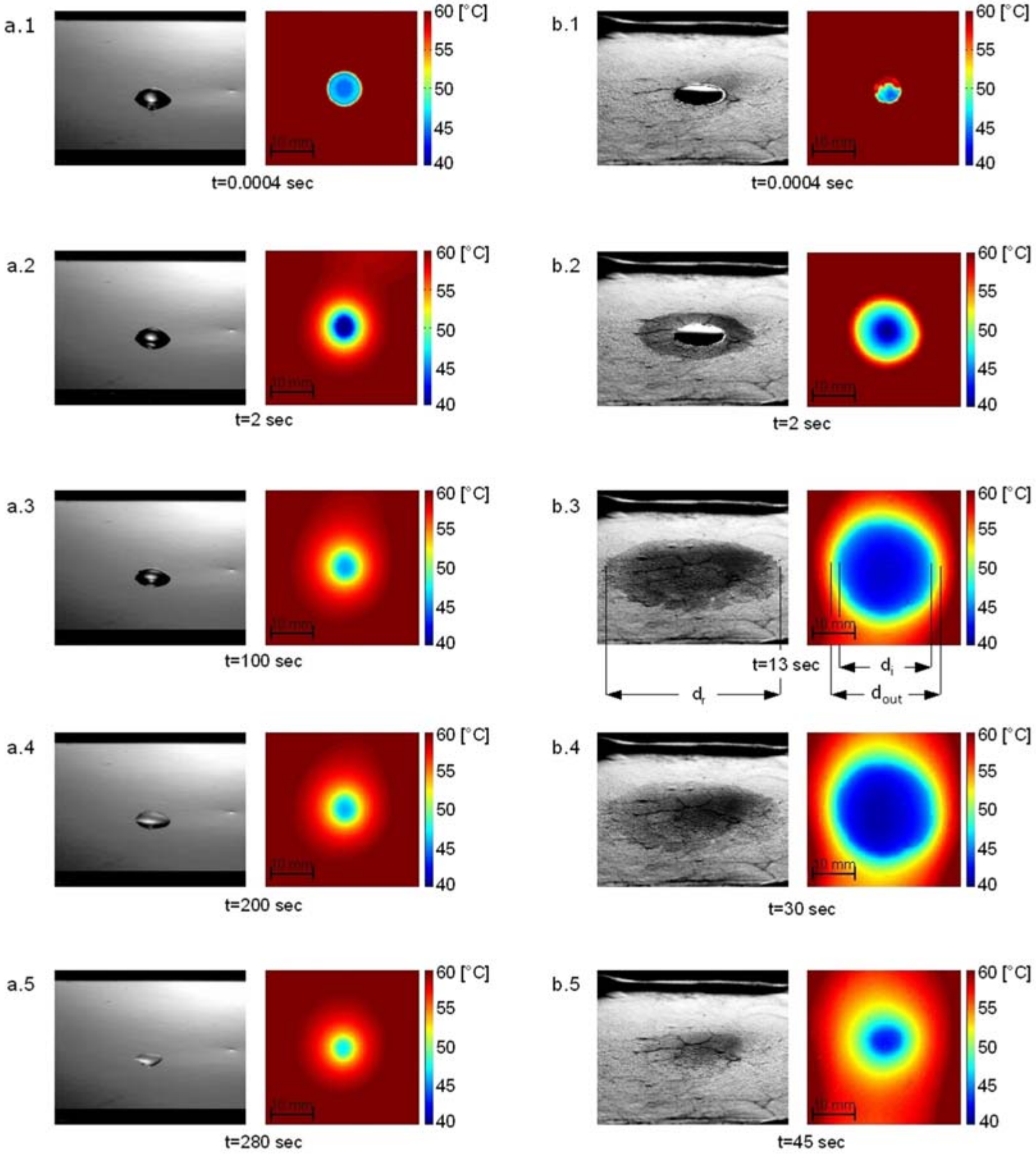

FIG. 5. Drop evaporation on a steel foil and on a nanofiber mat: a.1 – a.5 bare steel; b.1 – b.5 steel covered with PAN nanofiber mat, (mat thickness h=1.05 mm).

Figure 5 (b.1) shows the end of the spreading stage after drop impact on nanofiber mat, when the contact line of the drop is pinned in the spread- out configuration. The corresponding image of the temperature field demonstrates that at this early stage after drop impact, an evenly cooled area underneath the drop has not developed yet. Water penetration through the nanofiber mat thickness is not complete.

The entire process can be subdivided into three phases, which were observed for all polymer nanofiber mats used in these experiments. The first phase corresponds to the growth of the cooled area. After the spreading stage is over, the temperature of the back side of the foil is significantly reduced. However, the liquid does not remain at rest after the drop contact line had been pinned but rather starts to spread in the nanofiber mat outside the area encircled by the contact line, as can be seen in Fig. 5 (b.2). Water spreading inside the mats occurs in an almost axisymmetric manner. The maximum diameter of the cooled area in the case shown in Fig. 5 is about 12 times larger than the pre-impact diameter of the drop and takes a value of about 24 mm. During this process, the temperature of the foil underneath the wetted area of the nanofiber mat continues to change. Namely, the growth of the wetted area inside the nanofiber mats leads to a continuous reduction of temperature of the cooled area. When a maximum size of the wetted spot has been achieved, the temperature attains a constant low value which is nearly uniform over the entire cooled area, see the image in Fig. 5 (b.3).

In the following second stage the evaporation process is comparable to that taking place on an uncoated foil. For the case shown in Fig. 5 the maximal size of the wetted spot does not change during about 20 seconds and the temperature of the cooled area does not change significantly either. During this time the intensity of the dark colored area visible in the high-speed images in Fig. 5 (b.3 and b.4) is reduced, which indicates that an additional evaporation cooling occurs over the entire wetted area.

The shrinkage of the cooled area, which corresponds to the shrinkage of the wetted spot, signifies the third and last phase of drop evaporation on a nanofiber mat. After reaching a low threshold of moisture content, the wetted area begins to shrink while the temperature of the cooled area still does not change. The observations at this stage would not have been possible without using an infrared camera. Since the darker coloring of the wetted area in the CCD images fades with increasing time, the complete evaporation process cannot be observed using this as an indicator. The infrared images allow one to observe that the shrinkage process occurs continuously, as documented by a monotonous reduction of the diameter of the cooled area. The shrinkage was practically axisymmetric, which corresponds to the most intensive evaporation over the wetted spot perimeter.

If one compares the evaporation process on a bare steel foil and the foil coated with nanofibers, three differences can be observed. First, the cooled area is about four times larger with the nanofiber mat than on the uncoated foil. Second, the minimum temperature at which the evaporation occurs is about 7 °C lower for the nanofiber mat than for the bare steel foil Third, the evaporation time is about six times shorter on the nanofiber mat for the same drop size.

C. Definition of the characteristic spreading diameter

The drop spreading inside nanofiber mats was determined on the basis of the infrared images. Due to the thermal conduction in the foil the decrease of the foil temperature occurs not only underneath the locally wetted area where evaporation takes place but also in the surrounding area. Therefore, a comparison of the visible wetted area in the CCD images and the temperature field images was necessary in order to identify the correct borders of the cooled area corresponding to the wetted spot.

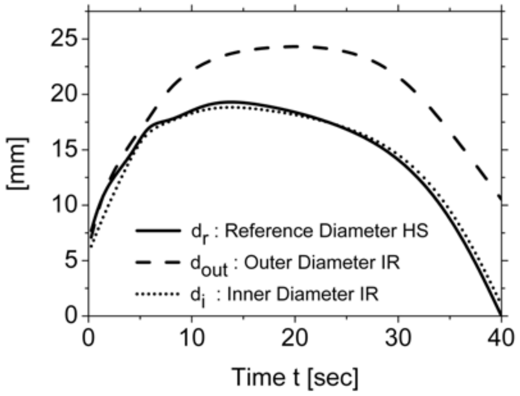

FIG. 6. Comparison of diameters of the wetted area evaluated using the high-speed (HS) and infrared (IR) images. The diameters d_r, d_{out}, and d_i are defined in Fig. 5 (b.3).

In Fig. 6 three different diameters selected for the comparison are shown; d_r is the diameter of the visible wetted area in the CCD images, d_i and d_{out} are the diameters of the two most significant temperature differences in the infrared images. They were measured manually for ten frames and plotted against time. This procedure was repeated for three measurements on different foils to verify the results. Figure 6 demonstrates that the diameter of the optically visible wetted area recorded by the CCD camera (d_r) corresponds in the IR images to the inner diameter d_i of the intense dark area, i. e. of the area which is cooled down to an almost uniform low temperature. It can be assumed, that the evaporation is taking place in this area and that the further temperature reduction in the surrounding area (d_{out}) is caused by thermal conduction in the foil.

A fixed threshold was chosen to convert the images from the infrared camera to determine a typical diameter of the wetted spot. It is emphasized that this procedure was not used during the initial phase when the water from the drop was still filling the pores directly at the impact location. The duration of that phase was in the range of 0.02-0.3 sec after drop impact for different mat thicknesses. For this time span, the diameter was set to zero, which explained the steep increase of d_i at the early stage after drop impact in Fig. 6.

3. EXPERIMENTAL RESULTS AND DISCUSSIONS

A. Water spreading inside nanofiber mats

The hydrodynamics of drop impact on nanofiber mats is essentially characterized by two features: the pinning of the contact line in the spread-out configuration and the further drop imbibition of pores outside the area encircled by the contact line. To elucidate peculiarities of the latter in more detail, the mat thickness, the initial foil temperature and the drop impact velocity were varied in the experiments. In the following, the diameter of the wetted area is scaled by the initial drop diameter d_0, $d_n = d/d_0$, whereas time t is measured from the drop impact moment. The experiments were performed with nanofiber mats of thicknesses in the range from h = 0.25 mm to 1.05 mm for the PAN samples, and from h = 0.15 mm to 1.75 mm for the PAN+CB samples.

The phenomenon of water imbibition in the nanofiber mats has been observed for all samples used. In all cases water spread almost axisymmetrically, with the maximum spreading diameters in the range $d_{n,max}$ = 9 to 15. The imbibition kinetics were different for various mats. That manifested itself in different time intervals required to reach $d_{n,max}$, different values of the full spread-out diameter d_{max}, as well as in different overall time spans for complete evaporation. To demonstrate this, four examples have been chosen. The nanofiber mats are, correspondingly, PAN samples of the thicknesses h=0.25 mm, 1.05 mm and 1.5 mm, as well as a very thin PAN+CB sample of the thickness of h=0.15 mm.

In Fig. 7 the curves $d^2(t)$ and $d[d^2(t)]/dt$ illustrate the evolution of the cooled area (divided by $\pi/4$) at an initial foil temperature of 60°C. It is seen that the spreading scenarios are similar for the different mat thicknesses. The spreading inside the mats begins with a high velocity which then continuously decreases until the spreading diameter reaches its maximum. In the following, the spreading diameter stays at a plateau, whereas the spreading velocity is almost zero. The shrinkage of the cooled area begins then with a low velocity magnitude, which increases with decreasing of the area.

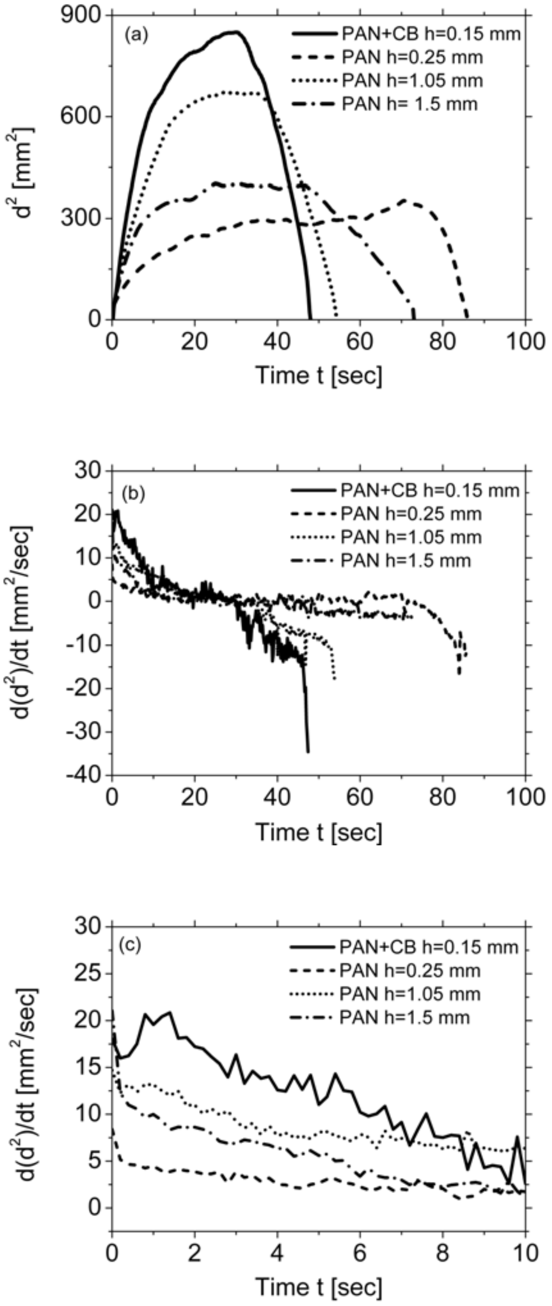

FIG. 7. Evolution of the cooled area (divided by π/4) in time at an initial foil temperature of 60°C. (a) d^2 versus time. (b) The derivative $d(d^2)/dt$ versus time. (c) The initial interval of the $d(d^2)/dt$ zoomed in.

The shortest process was observed for the thinnest mat produced from PAN+CB with the thickness of h = 0.15 mm. In that case the entire evaporation process took about 48 sec, while it takes nearly 300 sec on a bare steel foil under the same experimental conditions. The maximum spread-out diameter of the cooled area in the case of h = 0.15 mm was about 15 times larger than the pre-impact drop diameter, which corresponds to $d_{max} = 30$ mm. The time span corresponding to the plateau in $d^2(t)$ was about 20 sec. A similar result was obtained for the PAN nanofiber mat with the thickness of h = 1.05 mm. In the latter case, the maximum spreading diameter d_{max} was about 12 times larger than the initial drop diameter d_0, the time span corresponding to the plateau in $d^2(t)$ was about 30 sec and the entire evaporation time was about 55 sec. In the case of the thickest PAN mat with h = 1.5 mm the maximum diameter of the wetted spot was about 9 times larger than the pre-impact drop diameter d_0, the time span corresponding to the plateau was about 40 sec, and the entire evaporation took about 75 sec. In the case of the PAN nanofiber mat with the thickness of h=0.25 mm, in contrast to the previously discussed cases, exhibited a relatively low spread-out diameter equal to about seven times d_0 (Fig. 7a). The time span of the maximum spreading configuration was about 70 sec, which led to the longest measured entire evaporation time of 85 sec.

The large differences in the maximum spreading diameter for the thin PAN+CB mat compared with the thinnest PAN mat can be explained by different properties of the two materials. By adding carbon black particles to the polymer solution the roughness of individual nanofibers is increased (compare Figs. 1 and 2). The wettability properties are also affected by the carbon black particles.

The second parameter that was varied in these experiments was the initial foil temperature. Water penetration and spreading inside the mats occur for all nanofiber mats for the initial foil temperatures up to 120 °C. As the initial foil temperature increased, the maximum spreading diameter, as well as the evaporation time decreased, since the evaporation rate increased. The overall pattern of water spreading inside nanofiber mats was not affected by the initial foil temperature, as Figs. 8 a,b show in comparison with Fig. 7 a.

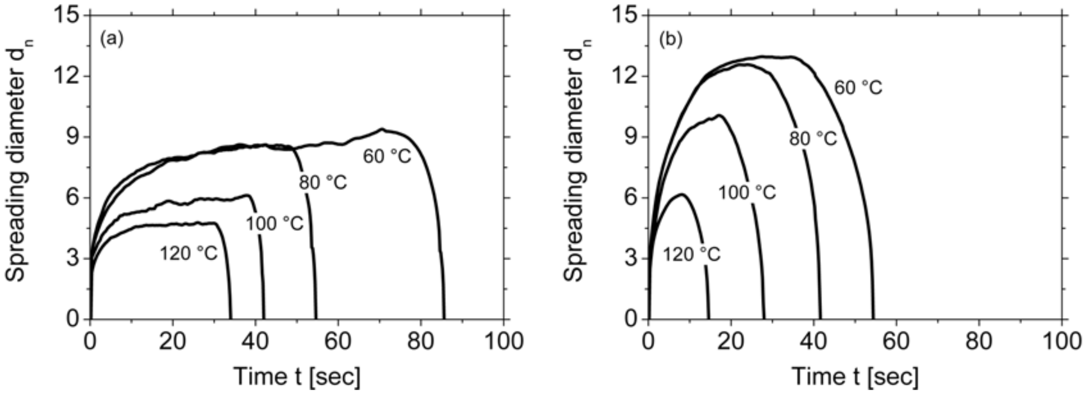

FIG. 8. Spreading diameter versus time for different initial foil temperatures. (a) PAN nanofiber mat with the thickness of h=0.25 mm; (b) PAN with h=1.05 mm.

For h = 1.05 mm at all the initial temperatures, drops spread very rapidly inside the mats and the dependence of the diameter of the cooled area on time had an almost parabolic shape over the entire process, Fig. 8b. On the other hand, for a lower mat thickness of h = 0.25 mm, water spreads with a lower speed inside the mats and $d_{n,max}$ is smaller for the investigated temperatures (Fig. 8a). Moreover, not only the curves $d_n(t)$ were similar at the increasing foil temperatures but also the wetted spot shapes were similar at the moment of the largest spread-out. Note the difference between the curves $d_n(t)$ for the two initial temperatures 60 °C and 80 °C in Fig. 8a. At these temperatures the $d_n(t)$ curves are almost identical up to t = 50 sec, whereas the evaporation time is significantly shorter for 80 °C. A reduction of the maximum diameter becomes visible only at about 100 °C. This result can be explained by the intensification of the evaporation process at higher temperatures. This is further corroborated by Fig. 9 where d_{max} normalized by $d_{max,60}$ (at the initial temperature 60 °C), $d_{max}/d_{max,60}$, is plotted versus the initial foil temperature T_F .

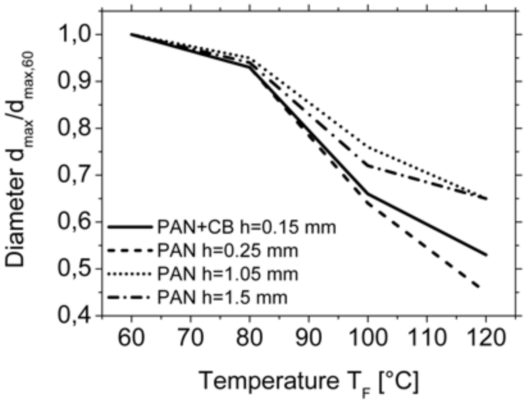

FIG. 9. Reduction of the relative maximum spreading diameter with the increasing initial foil temperature.

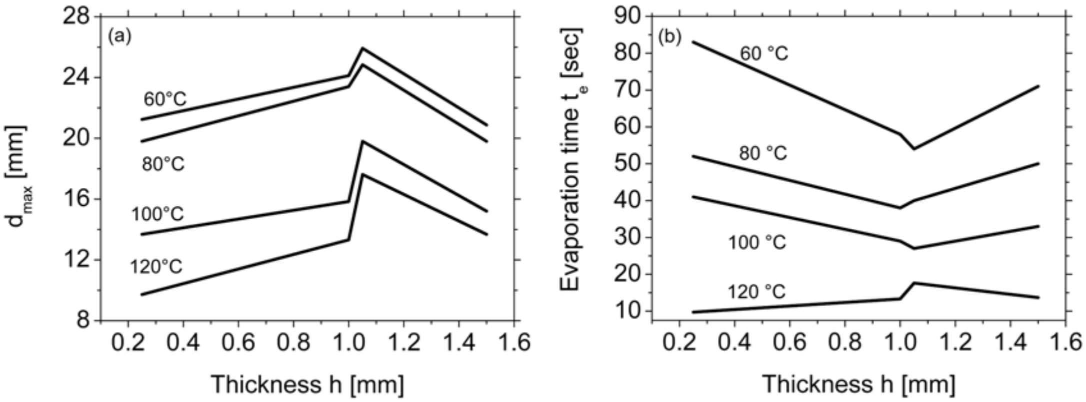

FIG. 10. (a) Maximum spreading diameter and (b) the corresponding evaporation time versus nanofiber mat thickness.

The data which allow evaluation of the relation between the maximum spreading diameter, the mat thickness and the corresponding evaporation time in the temperature range of 60-120 °C are shown in Fig. 10. It is seen that in the range of 60-100 °C there exists an optimal mat thickness of about 1 mm, which corresponds to the shortest evaporation time; hence the highest heat flux. Moreover, in the temperature range 60-120 °C there exists a mat thickness corresponding to a maximal value of d_{max}. It can be seen that, apart from the experiment performed at 120 °C, the evaporation time decreases with increasing maximum spreading diameter at a constant initial foil temperature. This can be explained by the increase of the liquid-gas interface area with an increase of the spreading diameter. The total evaporation rate increases and the evaporation time decreases with an increase of the liquid-gas interface area. The change of the trend for the initial foil temperature of 120 °C can be explained by possible inception of boiling in the nanofiber mat. One conceivable reason of the non-monotonic dependence of the maximum spreading diameter on the mat thickness can be the different impregnation behavior for thin and thick mats. In the case of thin mats the impregnation is mainly two-dimensional, since the thin mats are filled during drop impact through the entire depth. For mats thicker than h=1 mm the impregnation process can be assumed to be three-dimensional, where wettability driven filling in the third direction (in depth) occurs. With increasing of the mat thickness the moisture flux in the depth direction increases and d_{max} decreases. The decrease of the maximum spreading diameter with decreasing mat thickness for the thin mats can be attributed to the wall effects."

The third parameter that was varied in the experiments was the impact height H and the corresponding drop impact velocity. It was observed that this parameter mainly influenced the drop spreading before the contact line had been pinned, rather than further mat imbibition. It is known that in the case of drop impact onto a smooth dry substrate increasing the impact velocity leads to the enlargement of the spreading diameter [14]. However, as seen in Fig. 11, the rate of water imbibition and evaporation inside nanofiber mats were almost unaffected by the impact velocity at different initial foil temperatures.

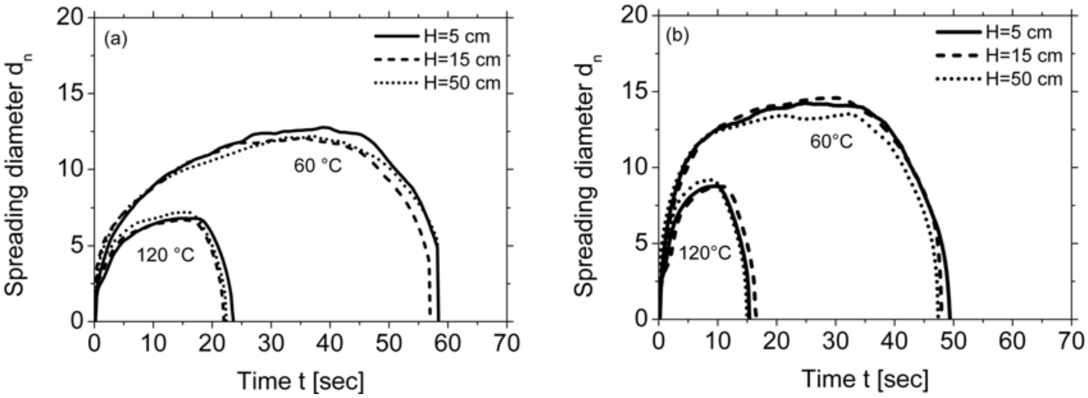

FIG. 11. Spreading diameter versus time for different impact heights. (a) PAN+CB nanofiber mat with thickness h=0.15 mm; (b) PAN with h=1.00 mm.

B. Cooling efficiency

Figure 12 (a,b) shows the foil temperatures at the impact axis for different nanofiber mats and the initial foil temperatures 60 °C and 100 °C. It can be seen that the foil temperature underneath the impact point drops almost instantaneously by about 25 °C for the initial foil temperature of 60 °C and by about 45 °C for 100 °C. After that, it stays almost constant during the whole evaporation process. It is emphasized that the minimum temperature at which the evaporation takes place, is between 3°C and 5°C lower for all nanofiber mats than in the case of an uncoated steel foil. This is demonstrated in Fig. 13a. Furthermore, the evaporation time is significantly shorter for all nanofiber mats, than that for an uncoated steel foil, as is seen in Fig. 13b. This diagram also elucidates the correlation between the maximum spreading diameter and the evaporation time. The samples in Fig. 13b are the same as in Fig. 7a from which the maximum diameters of the cooled area can be determined.

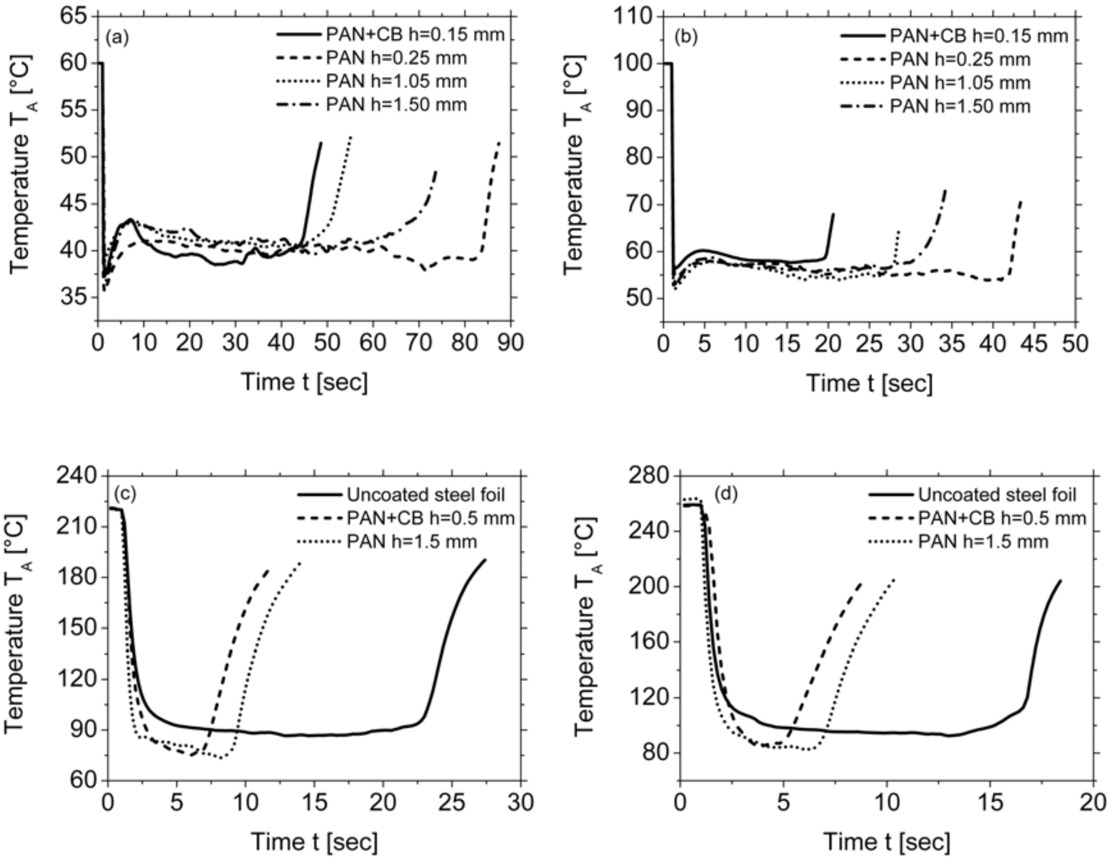

FIG. 12. Foil temperature under the drop impact point, T_A, for different nanofiber mats and different initial temperatures. (a) The initial foil temperature $T_{foil,init}$=60 °C; (b) $T_{foil,init}$=100 °C; (c) $T_{foil,init}$=220 °C; (d) $T_{foil,init}$=260 °C.

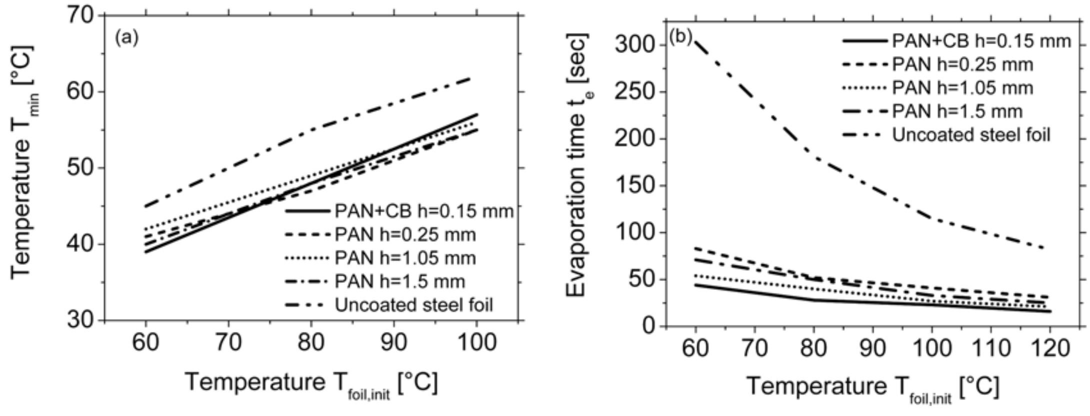

FIG. 13. Cooling efficiency of nanofiber mats as compared to the uncoated steel foil. (a) The minimum temperature and (b) the evaporation time versus the initial foil temperature.

The evaporations times in the case of the PAN+CB mat with the thickness of h = 0.15 mm, are the shortest ones for all temperatures, while at the same time this mat leads to the largest spreading diameters for all temperatures. The same observation is relevant for all the other mats, i.e. the larger spreading diameters result in shorter evaporation times as is also corroborated by Fig. 7a.

At higher foil temperatures 220 and 260 °C the temperature drop immediately underneath the impacting point can be as high as 140 and 180 °C, respectively.

4. EVALUATION OF THE HEAT FLUX AND COMPARISON WITH THE EXPERIMENT

A. Water spreading and penetration into pores

Velocity of penetration of liquid into pores of nanofiber mats was studied first in [9] in the framework of the planar problem using the Cauchy formula from the complex analysis, which was reduced in that case to Poisson's integral formula for the upper half-plane. In the present subsection, a more realistic axisymmetric case of dynamic penetration of liquid is tackled. In our experiments drop diameters are typically of the order of $d_0 \approx 10^{-1}\,\mathrm{cm}$, whereas the pore sizes are of the order of 10^{-3} cm. Therefore, drop impact onto a single pore can be imagined as an abrupt impact of a solid wall with a cylindrical orifice in the middle onto an upper half-space filled with water. A plane at z = 0 with the cylindrical orifice in the middle at $0 < r < a_0$ (where r and z are the radial and axial cylindrical coordinates centered at the orifice center and $a_0=d_0/2$) imposes a pressure impulse on the liquid filling the upper half-plane z> 0. The pressure impulse $\Pi = \lim\limits_{\substack{\tau \to 0 \\ p \to \infty}} \int_0^{\tau} \Delta p dt$ (where pressure $\Delta p \to \infty$ and the impact duration $\tau \to 0$) is of the order of one. The pressure impulse is applied at $r \geq a_p$, $z = 0$ to the liquid filling the upper half-plane where a_p is the pore radius. Flows arising in response to the pressure impulse are known to be potential, with flow potential $\phi = -\Pi / \rho_w$ being a harmonic function [15] (ρ_w is liquid, water, density). Its value over the solid wall $r \geq a_p$, $z = 0$ at the moment of impact was evaluated in [9] as $\varphi = -V_0 d_0$ where V_0 is the drop impact velocity.

The axisymmetric Laplace equation for the potential reduces to

$$\frac{1}{r}\frac{\partial}{\partial r}\left(r\frac{\partial \varphi}{\partial r}\right) + \frac{\partial^2 \varphi}{\partial z^2} = 0 \tag{1}$$

Solution for liquid is searched for $0 \leq r \leq \infty$, and $z \geq 0$, and the potential distribution in the liquid in contact with the wall is posed in the form

$$\phi|_{z=0} = f(r) = \begin{cases} 0, & 0 \leq r < a_p \\ -V_0 d_0, & a_p < r < \infty \end{cases} \tag{2}$$

(see Fig. 14).

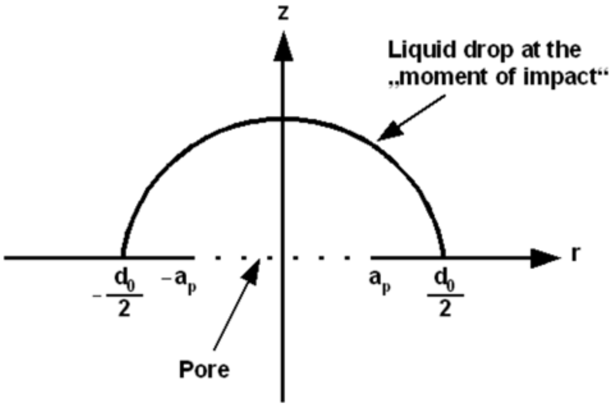

FIG. 14. Schematic of a liquid drop impact onto a single pore in the axisymmetric case.

The additional boundary conditions required are the following:

$$\varphi|_{r=0} < \infty \text{ and } \varphi < \infty \text{ over } r \to \infty \text{ and } z \to \infty \tag{3}$$

To solve the problem (1)-(3) and find φ(r,z), the method of separation of variables is applied. The solution of Eq. (1) satisfying the boundary conditions (3) has the following form:

$$\varphi = \int_0^\infty M_\nu e^{-\nu z} J_0(\nu r) d\nu \,, \tag{4}$$

where M_ν is an unknown function. This function can be determined from the boundary condition (2) using the following relation:

$$M_\nu = \nu \int_0^\infty f(\zeta)\zeta J_0(\nu\zeta) d\zeta = V_0 d_0 a_p J_1(\nu a_p), \tag{5}$$

where ζ is the dummy variable.

Then, Eq. (4) yields

$$\varphi(r,z) = V_0 d_0 a_p \int_0^\infty J_0(\nu r) J_1(\nu a_p) e^{-\nu z} d\nu \tag{6}$$

The velocity component $V_z = \partial\varphi / \partial z$, which yields at z=0 using Eq. (6),

$$V_z \Big|_{z=0} = -\frac{V_0 d_0}{a_p} \int_0^\infty \zeta J_1(\zeta) J_0(r\zeta/a_p) d\zeta \tag{7}$$

At z=0 and r=0, correspondingly,

$$V_z \Big|_{\substack{z=0 \\ r=0}} = -\frac{V_0 d_0}{a_p} \int_0^\infty \zeta J_1(\zeta) d\zeta \tag{8}$$

However, according to [16]

$$\int_0^\infty \zeta J_1 d\zeta = \int_0^\infty J_0(\zeta) d\zeta = 1 \tag{9}$$

Then, Eqs. (8) and (9) yield

$$V_z\Big|_{\substack{z=0\\r=0}} = \frac{-2V_0 d_0}{d_p} \tag{10}$$

where the pore diameter $d_p=2a_p$.

The velocity minimum is expected at the pore center, where $\left|\left(V_{z,\text{pore}}\right)_{\min}\right| = U$

$$U = \frac{2V_0 d_0}{d_p} \tag{11}$$

As expected, in the axisymmetric case (11), the value of U is even higher than that for the planar case [9] where it was $U=(4/\pi)(V_0 d_0)/d_p$.

According to the results obtained, the r-component of the velocity vector over the opening vanishes, i.e. the flow through it right after drop impact will be strictly anti-parallel to the z axis. The central part of the flow through the pore opening will not be affected by viscous forces when $\rho_w U^2 >> \mu_w U / a_p$ (where ρ_w and μ_w are the liquid density and viscosity, respectively). That is equivalent to the condition that the Reynolds number $Re_p = \rho_w U a_p / \mu_w >> 1$. Taking for the estimate $d_0 \approx 10^{-2} - 10^{-1}$ cm, $d_p = 2a_p = 10^{-3}$ cm and $V_0 = 1$ m/s, we find that $U = 10 - 10^2$ m/s $>> V_0$ and for water $Re_a = 10^2 - 10^3$. Therefore, in this case the high value of U will not be affected by viscosity even for such small pores, even though the flow close to the edges of the pore opening will be affected by viscosity. As mentioned in [9], drop penetration simultaneously in several pores will diminish the value of U. Still, a large disparity between d_0 and d_p will result in $U >> V_0$.

The high values of the velocity U compared to the drop impact velocity V_0 stem from the accumulation of the kinetic energy of a large mass of liquid in flow through a narrow pore and are reminiscent of the formation of shaped-charge (Munroe) jets [9].

The predicted values of the flow velocity through the pore $U \sim 10-10^2$ m/s are much higher than the speed of the wettability-driven impregnation of pores given by the Lucas-Washburn formula [17]. Accordingly, filling pores in the nanofiber mat of the thickness $h \approx 10^{-1}$ - 1 mm after drop impact takes not more than $t_f \approx h/U \approx 10^{-4}$ s. On the other hand, complete drop spreading over the mat lasts for about $t_s \approx d_0/V_0 \approx 10^{-3}$ sec [14, 18], which means that filling pores is an almost instantaneous process on the background of drop spreading ($t_f \ll t_s$).

B. Heat transfer

The characteristic time of cooling of the metal foil right under the drop (cooling stage 1) is of the order of $t_{foil,init}=h_f^2/\alpha_{steel}$, where h_f=50 μm is the foil thickness and $\alpha_{steel}=4\times10^{-6}$ m^2/s is the thermal diffusivity of steel. This time $t_{foil,init}= 6\times10^{-4}$ s, which is shorter than the time of spreading, and thus cannot be a limiting factor for the foil cooling.

The characteristic time of drop heating can be estimated as $t_{drop,init}=h_{drop}^2/\alpha_w$, where $\alpha_w=1.4\times10^{-7}$ m^2/s is the thermal diffusivity of water. The thickness of the spreading drop initially varies in time as $h_{drop} \sim t^{-2}$ [19,20] and then reaches the residual value $h_{drop,resid} \approx d_0 \mathrm{Re}^{-2/5}$ [21] where the Reynolds number Re= d_0V_0/ν_w, where ν_w is the liquid viscosity. Since the Prandtl number of water is larger than unity, the thickness of the thermal boundary layer in the droplet is smaller than the thickness of the viscous one. Therefore, the residual drop thickness can be safely used for the estimation of the initial drop heating. The residual film thickness of the drop under our experimental conditions is approximately 75 μm. Therefore, the drop heating time can be evaluated as $t_{drop,init} \sim 10^{-2}$ s.

The initial stage of foil cooling has been characterized using time resolved temperature measurements with sampling rate of 1 kHz. The measurement results for PAN + CB nanofiber mats are shown in Fig. 15.

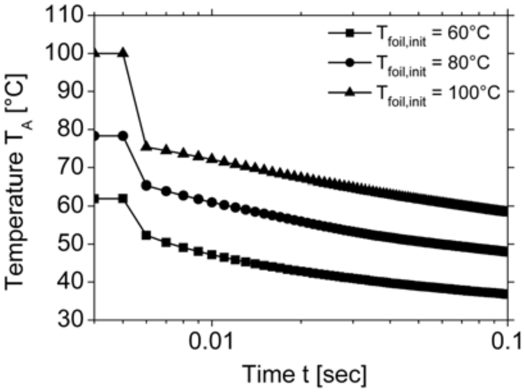

FIG. 15. Initial stage of cooling of a foil coated by the PAN +CB nanofiber mat

The average heat flux at the initial stage 1 can be estimated as $q_{init} = \rho_{steel} c_{steel} h_{steel} \left| dT_{steel} / dt \right|$. Taking for the estimate ρ_{steel}=8000 kg/m^3, c_{steel}=500 J/(kg K) and h_{steel}=50 µm, we find the maximum measured values of q_{init} for PAN + carbon black coated plates in kW/cm^2 listed in Table 1. It should be noted that the precision of the heat flux measurements at this stage is bounded by the sampling rate.

Table 1. The initial heat flux q_{init}, [kW/cm^2] for PAN + CB coated foils.

Initial foil temperature	60 °C	80 °C	100 °C
Cooling rate of the foil, |d*T*/d*t*|, deg/sec	5770	7170	12800
Heat flux, kW/cm^2	0.12	0.14	0.26

It is emphasized that the heat removed at stage 1 comprises only about 0.1 to 1% of heat which will be removed after the whole drop evaporates. Indeed, $\left[\rho_{steel}\pi a_{spot}^2 h_{steel} c_{steel}\left(T_{foil,0}-T_{low,short}\right)\right]/\left[\rho_w (4/3)\pi a_0^2 L\right]=10^{-3}-10^{-2}$, where a_0 is the initial drop radius, and L is latent heat of evaporation.

1. Foil cooling at times t from the range $t_s < t < t_{drop,init}$

At times $t > t_s$ the temperature gradients in the foil under the spread-out drop can be neglected, and therefore the foil temperature can be estimated using the lumped capacity approximation. We assume that the main heat transfer mechanism is heat conduction between the cold water drop and the steel foil in the direction normal to the plane of the foil (the *z*-direction). According to the estimates in section IV.A, we assume that for $t > t_s$ the nanofiber mats at the impact location are fully soaked with water. Since the volumetric fraction of the nanofibers is small, it can be assumed in our simplified analysis that the fully soaked nanofiber mats have the properties of water. The thermal conduction in the liquid is described using the transient one-dimensional thermal conduction equation:

$$\frac{\partial T}{\partial t}=\alpha_w \frac{\partial^2 T}{\partial z^2}. \tag{12}$$

Equation (12) is solved subject to the following boundary condition at the foil:

$$\rho_{steel} c_{steel} h_{steel} \frac{\partial T}{\partial t}=k_w \frac{\partial T}{\partial z} \text{ at } z=0, \tag{13}$$

where k_w is the thermal conductivity of water, and ρ_{steel} , c_{steel} and h_{steel} are the density, specific heat and thickness of steel foil.

Equations (12) and (13) can be written in the dimensionless form using the following dimensionless variables:

$$t=\overline{t}\,\frac{\alpha_w c_{steel}^2 \rho_{steel}^2 h_{steel}^2}{k_w^2},\ z=\overline{z}\,\frac{\alpha_w c_{steel} \rho_{steel} h_{steel}}{k_w},\ \Theta\left(\overline{z},\overline{t}\right)=\frac{T-T_{drop,0}}{T_{foil,0}-T_{drop,0}}. \tag{14}$$

where subscript zero denotes the initial values.

The resulting dimensionless energy equation and boundary and initial conditions read

$$\frac{\partial\Theta}{\partial\overline{t}}=\frac{\partial^2\Theta}{\partial\overline{z}^2},\ \text{for } \overline{z}\geq 0,\ \overline{t}\geq 0 \tag{15a}$$

$$\frac{\partial\Theta}{\partial\overline{t}}=\frac{\partial\Theta}{\partial\overline{z}},\ \text{for } \overline{z}=0,\ \overline{t}>0 \tag{15b}$$

$$\lim_{\overline{z}\to\infty}\Theta=0,\ \text{for } \overline{t}\geq 0 \tag{15c}$$

$$\Theta\left(\overline{z}=0,\overline{t}=0\right)=1,\ \Theta\left(\overline{z}>0,\overline{t}=0\right)=1 \tag{15d}$$

The problem (15) is solved using the Laplace transform, which yields the following dimensionless dependence of $\Theta\left(\overline{z}=0,\overline{t}>0\right)=\Theta_{foil}(\overline{t})$ on $\overline{t}$

$$\Theta_{foil}=1+\sum_{j=1}^{\infty}\frac{(-1)^j\,\overline{t}^{\,j/2}}{\Gamma(1+j/2)},\qquad \frac{d\Theta_{foil}}{d\overline{t}}=\sum_{j=1}^{\infty}\frac{(-1)^j\,j\,\overline{t}^{\,j/2-1}}{2\Gamma(1+j/2)}. \tag{16}$$

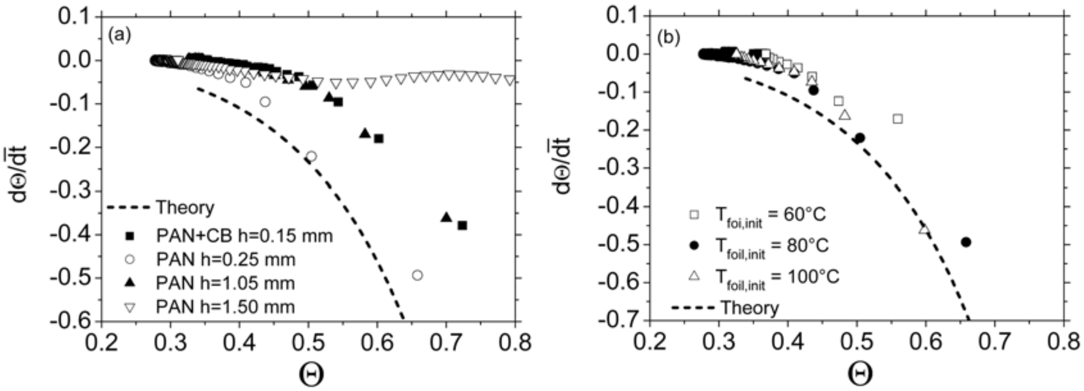

FIG. 16. Measured scaled rate of temperature evolution of the foil (the heat flux at the foil surface) in the range $t_s < t < t_{drop,init}$ in comparison with the theoretical predictions (16). (a) Different nanofiber mats at the initial temperature 60°C. (b) PAN nanofiber mat of h = 0.25 mm at different initial temperatures.

The theoretical prediction for the rate of Θ_{foil} variation (which is, in fact, the heat flux) is compared with the experimental data in Fig. 16 for different nanofiber mats and different initial temperatures of the foil. For the calculations the series (16) are truncated at the 51th term. The agreement of the theoretical results with the experimental data in Fig. 16 is reasonable. The closest agreement is observed for the PAN nanofiber mat of thickness h = 0.25 mm. Some deviation of the data from the theoretical predictions for other mats can be explained by the influence of the mats on the effective thermal properties of the medium in contact with the steel foil.

2. The lowest temperature of the foil at $t_s < t < t_{drop,init}$

The temperature of the foil T_{low} at times comparable with $t_{drop,init}$ can be estimated from the energy balance, neglecting the heat losses to air and drop evaporation:

$$\rho_{steel} c_{steel} h_{steel} \left(T_{foil,0} - T_{low}\right) = \rho_w c_w h_{drop,resid} \left(T_{low} - T_{drop,0}\right), \tag{17}$$

where the initial drop temperature is $T_{drop,0} = 25°C$ and c_w is the specific heat of water. The estimated values of T_{low} for the case of drop impact onto a bare steel foil are shown in Table 2 in comparison with the measured data. The agreement of T_{low} with the measured value $T_{low,short}$ ($T_{low,short}$ is the lowest temperature right after drop impact, cf. Fig. 11) is very good. In addition, Table 2 also contains the measured values of the temperature $T_{low,plateau}$ corresponding to the temperature plateau in Fig. 11.

Table 2. Measured data for the wet spot radius a_{spot}, and wet spot temperatures $T_{low,short}$ and $T_{low,plateau}$.

	Initial temp. [°C]	a_{spot} [mm]	$T_{low,plateau}$ [°C]	$T_{low,short}$ [°C]	T_{low} [°C] theory Eq. (17)
PAN+CB h=0.15 mm	60	14.4	39	37	
	80	13.5	48	45	
	100	9.5	58	56	
PAN h=0.25 mm	60	10.62	39	36	
	80	9.9	47	44	
	100	6.84	56	53	
PAN h=1.05 mm	60	12.96	40	38	
	80	12.42	45	43	
	100	9.9	56	53	
PAN h=1.5 mm	60	10.44	41	36	
	80	9.9	49	44	
	100	7.6	57	53	
Bare steel foil	60	3	45	37	38
	80	3	56	47	46
	100	3	62	57	54

At the second stage steel under the spread-out drop has the low plateau temperature $T_{low,plateau}$ (cf. Fig. 11), and the cooling process becomes different: heat is transferred mainly by conduction along the foil horizontally to the cold spot of radius a_{spot} at the center. This heat transfer sustains evaporation of the main part of the drop on the cold spot, and this is a long limiting process. Indeed, the thermal balance for such a process relates the conductive heat transfer to the latent heat of evaporation:

$$k_{steel} \frac{\left(T_\infty - T_{low,plateau}\right)}{a_{spot} \ln(W / a_{spot})} 2\pi a_{spot} h_{steel} \Delta t \approx \rho_w \frac{4}{3} \pi a_0^3 L \tag{18}$$

where k_{steel} is the thermal conductivity of steel, W is of the order of the foil size, and Δt the duration of drop evaporation.

Equation (18) yields

$$\Delta t = \frac{2}{3} \frac{\rho_w a_0^3 L \ln(W / a_{spot})}{k_{steel} h_{steel} \left(T_\infty - T_{low,plateau}\right)} \tag{19}$$

Taking for the estimate ρ_w=1000 kg/m^3, k_{steel}=16 W/(m K), L=2260 kJ/kg and W=2.5 cm, as the foil width, one finds from Eq. (19) the values of drop evaporation time Δt listed in Table 3 in comparison with the experimental results.

Table 3. Measured and calculated evaporation time, [sec].

	60 °C		80 °C		100 °C	
	Measured	Calculated	Measured	Calculated	Measured	Calculated
PAN+CB h = 0.15 mm	44	49	28	36	23	43
PAN h = 0. 25 mm	83	77	52	53	41	55
PAN h = 1.05 mm	54	62	40	38	27	39
PAN h = 1.5 mm	71	86	50	56	33	52
Bare steel foil	303	266	181	166	115	105

Equation (19) incorporates the effect of nanofibers through the value of a_{spot}. Nanofiber mats icrease a_{spot} and thus decrease Δt. The agreement of the measured and predicted values of Δt is fairly good.

5. CONCLUSION

Drop spreading after impact on polymer nanofiber mat is almost instantaneously followed by water penetration into pores, after which heat is removed from the underlying hot stainless steel foil, corresponding to the latent heat of water evaporation in direct contact with the foil. At the first stage of cooling, the heat flux is of the order of up to 0.3 kW/cm^2, which is characteristic of spray cooling in general. At the second stage heat is removed by conduction along the foil towards the cold central spot which appeared at stage 1, and only then is used for water evaporation. The drop imbibition and evaporation introduce a limiting stage which prolongs the drop evaporation process to several tens of second and diminishes the overall heat flux. It is expected that the limiting stage can be significantly shortened with highly conductive metal nanofibers instead of the polymer ones used in the present work. The work on drop cooling through metal nanofibers is currently underway and will be reported separately.

ACKNOWLEDGMENTS

The authors would like to thank PhD students Matthias Winter (TTD) and Olympia Kyriopoulos (SLA) for their help in design and construction of the experimental setup. Support of the Center of Smart Interfaces (Technische Universität Darmstadt) is greatly appreciated. YZ and ALY are also greatful for the partial support of their work by National Science Foundation through the Grant CBET-0966764. I.V.R. and C.T. acknowledge a partial support by DFG in the framework of Collaborative Research Center Transregio 75, subproject A4.

REFERENCES

1. L.P. Yarin, A. Mosyak, G. Hetsroni, *Fluid Flow, Heat Transfer and Boiling in Micro-channels*. Springer, Berlin, (2009).
2. S.G. Kandlikar, A.V. Bapat, *Heat Transfer Eng.* **28**, 911 (2007).
3. J. Kim, *Int. J. of Heat and Fluid Flow* **28**, 753 (2007).
4. Z.B. Yan, K.C. Toh, F. Duan, T.N. Wong, K.F. Choo, P.K. Chan, Y.S. Chua, *Appl. Therm. Eng.* **30**, 1225 (2010).
5. M. Visaria, I. Mudawar, *IEEE T COMPON PACK T* **32**,784 (2009).
6. R.M. Manglik, M.A. Jog, *J. Heat Transf.* **13**1, 121001 (2009).
7. M.R.O. Panao, A.L.N. Moreira, *Int. J. Therm. Sci.* **48**, 1853 (2009).
8. R. Srikar, T. Gambaryan-Roisman, C. Steffes, P. Stephan, C. Tropea, A.L. Yarin, *Int. J. Heat and Mass Transf.* **52,** 5814 (2009).
9. A.N. Lembach, H.B. Tan, I.V. Roisman, T. Gambaryan-Roisman, Y. Zhang, C. Tropea, A.L. Yarin, *Langmuir* **26,** 9516 (2010).
10. D.H. Reneker, A.L. Yarin, E. Zussman, H. Xu, *Adv. Appl. Mech.* **41,** 43 (2007).
11. D.H. Reneker, A.L. Yarin, *Polymer* **49,** 2387 (2008).
12. M.K. Tiwari, A.L. Yarin, C.M. Megaridis, *J. Appl. Phys.* **103,** 044305 (2008).
13. D.H. Reneker, A.L. Yarin, H. Fong, S. Koombhongse, *J. Appl. Phys.* **87,** 4531 (2000).
14. A.L. Yarin, *Annu. Rev. Fluid Mech.* **38,** 159 (2006).
15. G.K. Batchelor, *Introduction to Fluid Dynamics*. Cambridge University Press, Cambridge, 1967.
16. I.S. Gradshteyn, I.M. Ryzhik, *Table of Integrals, Series and Products*. 7th Edition, Elsevier, Amsterdam, 2007.
17. E.W. Washburn, *Proc. Natl. Acad. Sci.* 115 (1921).
18. R. Rioboo, M. Marengo, C. Tropea, *Exp. Fluids* **33,** 112 (2002).

19. A. L. Yarin, D. A. Weiss, *J. Fluid Mech* 283, 141 (1995).

20. I. V. Roisman, E. Berberović, and C. Tropea, *Phys. Fluids* **21**, 052103 (2009).

21. I. V. Roisman, *Phys. Fluids* **21**, 052104 (2009).